Hindawi
Advances in Civil Engineering
Volume 2021, Article ID 6640240, 17 pages
https://doi.org/10.1155/2021/6640240

Research Article

Influence of Dry Beach on the Dynamic Stability of Ash Storage Field: A Numerical Analysis

Fangtao She[1,2,3] **Chang Liu**[2] **Xiangang Zhou**[2] **Changjun Qi**[4] **and Jiulong Ding**[2,3]

[1]*State Key Laboratory of Eco-hydraulics in Northwest Arid Region, Xi'an University of Technology, Xi'an 710048, China*
[2]*Institute of Geotechnical Engineering, Xi'an University of Technology, Xi'an, Shaanxi 710048, China*
[3]*Shaanxi Provincial Key Laboratory of Loess Mechanics, Xi'an University of Technology, Xi'an 710048, China*
[4]*China JK Institute of Engineering Investigation and Design Co. Ltd., Xi'an 710043, China*

Correspondence should be addressed to Fangtao She; shefangtao@xaut.edu.cn

Received 2 December 2020; Revised 12 January 2021; Accepted 24 January 2021; Published 20 February 2021

Academic Editor: Jian Xu

Ash storage sites are a commonly used method of disposing fly ash, a byproduct of coal combustion, in China today, and when it accumulates to a certain height, serious geological hazards may occur as a result of seismic activity. In this study, an in situ standard penetration test was carried out on a constructed ash storage site in Northwest China to evaluate the potential for liquefaction of alluvial fly ash within the site, and the results show that dynamic liquefaction can occur within a newly constructed three-stage subdam. A numerical analysis of the influence of dry beach length on the dynamic response of the primary dams and subdams and an assessment of the extent of dynamic liquefaction in the ash storage field were carried out using the Wenchuan seismic waves as input ground motion. Numerical results prove that the acceleration within the ash storage field is relatively low in the original breccias layer and gradually increases with height, with the peak acceleration occurring in the vicinity of the third subdam and a decreasing trend from the subdams towards the ash storage field. As the length of the dry beach increases, the Peak accelerations in the ash storage area occur near the third subdams at larger dry beach length. Meanwhile, the acceleration in the ash storage area close to the surface gradually increases, and, significantly, the range where higher accelerations occur also becomes larger. The maximum horizontal displacements at different dry beach lengths occur at the crest of the third subdam and in the adjacent ash storage area. As the length of the dry beach increases, the maximum horizontal displacements show a certain decrease, but they occur progressively further away from the third subdam, so that, under dynamic action, the dams become safer. The extent of liquefaction decreases at larger dry beach length and extends further away from the third subdam into the ash storage area. It is, therefore, recommended that the length of the dry beach should not be less than 150 m for this ash storage site.

1. Introduction

China is a large coal-consuming country, producing hundreds of millions of tons of fly ash every year due to power generation, most of which come from the fly ash power boilers of large and medium thermal power plants. As a byproduct of coal combustion, fly ash is treated in a different way from other industrial waste residues due to the special nature of its chemical composition, and appropriate treatment methods should be chosen in order to minimize the environmental pollution and maximize the waste utilization [1]. Two main methods of handling fly ash both at home and abroad are integrated utilization and storage in ash storage sites. Especially in recent years, the use of fly ash to improve the engineering properties of materials in industries such as civil engineering and road construction has become an effective way to resource fly ash [2–4]. Although the utilization rate of fly ash is increasing every year, the overall utilization rate is low, and storage in ash storage sites is still the mainstay. This approach also faces several environmental pollution problems [5], e.g., air pollution caused by the wind-driven escape of bare fly ash from ash storage sites into the atmosphere and pollution of the surrounding soil and underground water bodies after leaching of harmful

chemicals from fly ash [6–8]. However, more importantly, there is also the risk of dam failure when fly ash accumulates to a certain height in the ash storage site [9]. In addition to destabilization due to heavy rainfall, severe geological hazards can be induced by seismic motion.

Extensive studies have been accumulated on the dynamic properties of fly ash in ash storage sites. Li et al. [10] analyzed the stress-strain characteristics of fly ash under consolidated-drained and consolidated-undrained conditions by means of a triaxial vibration test and found that relative density greatly influences the area of the liquefaction zone. Based on the dynamic effective stress analysis of the dam, Wang and Wang [11] determined the safety factor for sliding stability, and there is a large difference in the acceleration distribution coefficient along the dam height and slope, and the base frequency of the dam decreases as the dam softens. Hu [12] found, from the liquefaction and dynamic stability analysis of ash dams, that the dynamic instability will occur even without liquefaction zones in the ash dam during the seismic motion. Zhou et al. [13] found that the maximum pore water pressure was more sensitive to liquefaction than that occurring near the top of the dam and that these areas were more sensitive to liquefaction. Liu et al. [14] studied the dynamic properties of fly ash and silty clay on road base and concluded that the dynamic properties of fly ash were better than those of silty clay after three freeze-thaw cycles. Dong [15] found that the dynamic stress-strain relationship for soil-fly ash mixture can be approximated by the hyperbolic function, and the more the soil mixed, the higher the dynamic shear stress corresponding to the same shear strain. Wang [16] observed that dynamic strain of fly ash-treated soil grows at higher dynamic stress or at higher confining pressures, while the dynamic strength increases at higher contents of fly ash. Wang et al. [17] studied the constitutive model of improved loess by fly ash. Zhang et al. [18] investigated the dynamic performance of fly ash in view of the dynamic liquefication and softening of dynamic modulus. Li et al. [19] carried out dynamic torsional shear tests on the dynamic behavior of fly ash. Wei et al. [20] studied the dynamic properties of fly ash considering the influence of temperature. The above scholars have carried out valuable researches on the dynamic properties of fly ash. However, little research has been done on fly ash in ash storage areas, and because of its high accumulation, its safety cannot be neglected in case of earthquakes.

In order to study the dynamic stability of the ash storage field, field tests were carried out, and the liquefaction potential of the ash storage field was analyzed by means of standard penetration tests. Numerical analysis was used to investigate the dynamic response of the primary dam and subdams at different dry beach lengths, including acceleration, horizontal displacement, and the extent of dynamic liquefaction using a pore pressure level-based approach. The results of the study provide a basis for the evaluation of the dynamic safety of existing ash storage sites.

2. Field Tests

2.1. Overview of the Ash Storage Site. The ash storage site is located in the Gobi Desert at the northern edge of the Yinchuan Basin, where the Baolan Railway and National Highway 110 pass by, adjacent to the Yellow River in the east and overlooking the Helan Mountains in the west. The ash storage site adopts a stage-by-stage damming scheme, with a permeable primary dam constructed by local Gobi sand and gravel material, and the later stage adopting the upstream method of raising the dam with compacted ash. The maximum height of the primary dam is approximately 22 m. The first subdam is approximately 4.0 m. Currently, the ash site has a secondary subdam that was raised at the end of 2007 with a height of approximately 5 m, a crest elevation of 1124.30 m, and a restricted ash storage elevation of 1123.30 m. In 2010, a third subdam was raised with a height of 5 m, an upstream and downstream slope of 1:3.0, and a width of 4 m at the top of the subdam. The crest elevation and the limiting ash storage elevation are 1129.30 m and 1128.30 m, respectively, while, for the ash field drainage system, one reinforced concrete shaft-canal drainage channel was used, including two shafts with an inner diameter of 3.0 m and a height of 27.0 m and 23.0 m, respectively. The internal diameter and total length of the culvert drainage channel are 1.6 m and 600 m, respectively. Geomembranes were used for the whole ash storage field to prevent infiltration of ash and polluted groundwater, and the thickness of soil over the impermeable membrane is 0.3 m. Figure 1 presents the schematic diagram and photo of the ash storage field.

2.2. Engineering Geological Condition of the Ash Storage Site. The ash storage site is located between the fold fracture zone on the western margin of the Ordos Plateau and the Alashan Plot, which is the contact zone between the Yinchuan Sedimentary Plain and the rising mountains of the Inner Mongolian Axis, and belongs to the overlapping area of the Yinshan Latitudinal Tectonic Belt, the Helan Mountains Longitudinal Tectonic Belt, and the New Huaxia Tectonic System. The geological complexity of the area and the strong neotectonic movements also make it an earthquake-prone area, but there are no active fractures in or near the ash storage site. According to the Seismic Intensity Zoning Map of China, the antiseismic fortification intensity of the ash field can be considered at 8 degrees, and the potential sources of earthquakes are all under the influence of near earthquakes. The ash field is high in the west and low in the east, and the geomorphological units belong to the high and low terraces in front of the Helan Mountains, and no adverse geological phenomena were seen.

The stratigraphy in the ash storage field is dominated by fluvial deposits (Q_{3-4}^{P1}) and alluvial-fluvial deposits (Q_3^{a1+p1}). The stratum consists of clay, sandy, and gravel, and there are many mixtures and interlayers of different lithologies, but, in general, the gravelly soil is dominant. Table 1 lists the main stratum of the ash storage field. Due to the uniform stratigraphical division of the two terraces in the high and low parts of the ash storage field, the smaller net thicknesses of the interlayers and lenses are grouped together in the larger layers. Note that the former two types of soils were removed from the foundation before constructing the

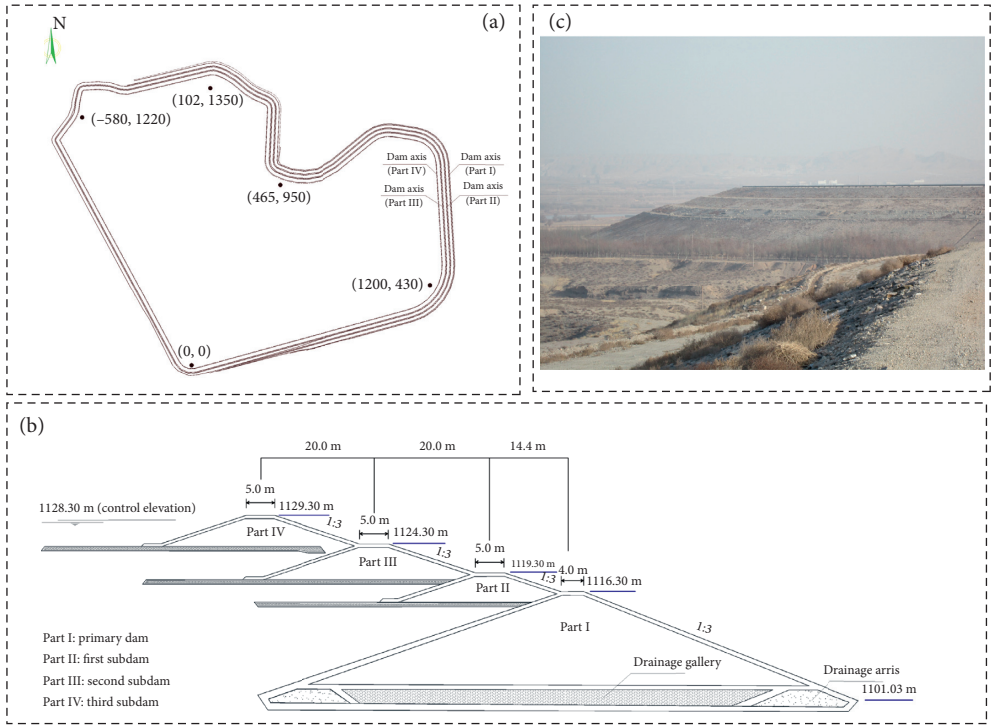

Figure 1: Schematic diagram and photo of the ash storage site. (a) The planar graph, (b) the cross-sectional graph, and (c) the photo of the ash storage field.

Table 1: Stratum of the ash storage field.

Stratum	Property	Distribution feature	Components
Breccias (Q_{3-4}^{P1})	Brownish red, medium dense, sorted, poorly rounded, angular, well graded	Widely distributed on terrace surfaces, with depth of 0.3–1.4 m	Mainly quartzite, quartz sandstone and granite which is moderately to strongly weathered (5–15 mm in size and the largest visible size 150 mm). The fill is mainly sand and clay soil, accounting for about 30–40%.
Silt soil (Q_{3-4}^{P1})	Brownish-yellow to pale yellow, slightly wet, slightly to medium dense, very uneven soil texture	High terrace frontage and some of the gully slopes and bottoms, otherwise sporadic, with great variation in thickness, about 0.4–9.6 m	Highly mixed, highly variable lithology, partly silt or silty clay, partly wetting collapsible
Breccias (Q_3^{a1+p1})	Mainly grey, greenish grey, brownish red and brownish yellow, dense, well rounded, subangular-subrounded, poor sorting and good grading	Widespread in the whole ash storage field with multilayers, with total depth of about 15 m	Mainly quartzite, granite, and quartz sandstone, moderately to strongly weathered (particle size 5–20 mm, and the largest visible size 500 mm). Horizontal stratification with the fill mainly medium and fine sand, accounting for about 20–30% of the total.

primary dam; the third type of soil was used as the main loading bearing layer.

2.3. Field Standard Penetration Tests. Twenty measurement points were selected to carry out standard penetration tests at the top of the third subdam, second subdam, and the ash storage field. For saturated sand and silt soils, when the soil is initially judged to be likely to be liquefied or the effects of liquefaction need to be considered, the standard penetration test may be used to further determine whether it is liquefied. Based on the Code for seismic design of buildings (GB 50011–2010), when the measured number of standard penetration hammers (uncorrected for rod length) N is less than the critical value N_{cr}, the soil should be judged to be liquefied; otherwise, it is not liquefied.

$$N_{cr} = N_0\beta\left[\ln\left(0.6d_s + 1.5\right) - 0.1d_w\right]\sqrt{\frac{3}{\rho_c}}, \quad (1)$$

where N_{cr} is the threshold value for the number of standard penetration hammers; N_0 is the reference value for the number of standard penetration hammers for soil liquefaction determination, which is equal to 12 for the tested region (the zone of eight degrees of intensity); d_s is the depth of standard penetration test (m); d_w is the groundwater level (m); ρ_c is the percentage of clay particle, which is equal to 3 for the cases of lower than 3 or sand; β is the adjustment factor, which can be taken as 0.80, 0.95, and 1.05 for the design seismic groups I, II, and III, respectively.

Table 2 lists the standard penetration test results for this ash storage field. It is evident that liquefaction zones are virtually absent in the second and third subdams, with a critical value occurring within the dam body at the subdam drainage mat. The other two critical areas are in the ash storage field of the second subdam below the third, which also indicates that no liquefaction areas are present in the dam body at all levels and that liquefaction areas may occur in the ash storage area.

Table 2: Standard penetration test results.

Location	Depth (m)	N	N_{cr}	Judgment
Third subdam	1	34	2	No
Third subdam	2	12	4	No
Third subdam	4	6	5	No
Third subdam	5	8	6	No
Ash storage field in second subdam	8	8	8	Critical
Ash storage field in second subdam	10	8	9	Yes
Second subdam	1	16	2	No
Second subdam	2	9	4	No
Second subdam	3	10	5	No
Second subdam	5	3	6	Yes
Third subdam	1	32	2	No
Third subdam	2	8	4	No
Third subdam	3	5	5	Critical
Third subdam	4	9	5	No
Third subdam	5	7	6	No
Second subdam	1	16	2	No
Second subdam	2	13	4	No
Second subdam	3	10	5	No
Second subdam	4	10	5	No
Second subdam	6	9	7	No

Note: in the judgment results, "No" denotes that the liquefication of test site is not required to be considered; "Yes" means that the test site is prone to soil liquefication; and "Critical" indicates that the liquefication of test site may occur but should be rationally considered in practical cases.

3. Numerical Scheme

3.1. Principle of Dynamic Finite Element Computation

3.1.1. Governing Equations. The key to the dynamic response analysis of an ash storage site is to solve the dynamic equation

$$[M]\{\ddot{u}\} + [C]\{\dot{u}\} + [K]\{u\} = \{R(t)\}, \tag{2}$$

where $[M], [C]$ *and* $[K]$ are the mass matrix, damping matrix, and stiffness matrix, respectively; $\{R(t)\}$ is the seismic dynamic load; $\{\ddot{u}\}, \{\dot{u}\}, \{u\}$ are the vectors of nodal acceleration, velocity, and displacement, which are relative to the bedrock.

The mass matrix is a collection of the mass matrices of the individual elements, where the elemental acceleration distributions are identical, and each of the four nodes of each element bears a quarter of the element mass, i.e., calculated using the centralized mass method

$$[M]^e = \int_{\Omega^e} \rho [\psi]^T [\psi] \mathrm{d}\Omega, \tag{3}$$

where $[\psi]$ is the matrix of the function ψ_i, equal to zero when the node is distributed in the region i; otherwise, it is 1; ρ is the unit density, and Ω_e is the unit volume domain.

The Rayleigh damping matrix was used to assemble the overall damping matrix

$$[C] = \lambda\omega[M] + \frac{\lambda}{\omega}[K], \tag{4}$$

where λ is the damping ratio of the element; ω is the fundamental frequency of the dam.

The calculation of the stiffness matrix $[K]$ is identical to the static formula except that the Young's modulus E is replaced by the shear modulus G in the calculation of the unitary elasticity matrix. The load vector $\{R(t)\}$ is calculated using the following equation:

$$\{R(t)\} = -[E_x]\ddot{\delta}_{gx}(t) - [E_y]\ddot{\delta}_{gy}(t), \tag{5}$$

where $\ddot{\delta}_{gx}(t), \ddot{\delta}_{gy}(t)$ are the seismic accelerations acting on bedrock in both horizontal and vertical directions. Only the horizontal seismic acceleration is taken into account in this calculation, once the latter term is 0. $[E_x], [E_y]$ are the centralized quality matrix of nodes, as calculated by

$$[E_x] = \begin{bmatrix} m_1 & & & & \\ & 0 & & & \\ & & m_2 & & \\ & & & \cdots & \\ & & & & m_n \\ & & & & & 0 \end{bmatrix},$$
$$[E_y] = \begin{bmatrix} 0 & & & & \\ & m_1 & & & \\ & & 0 & & \\ & & & \cdots & \\ & & & & 0 \\ & & & & & m_n \end{bmatrix}, \tag{6}$$

where m_i ($i = 1$ to n) is the centralized quality of node i. The equations were calculated using the Wilson theta implicit integration method in a nonlinear iterative manner.

3.1.2. Method of Calculating the Dynamic Shear Modulus and Damping Ratio. The Hardin–Drnevich model assumes a hyperbolic relationship between dynamic shear modulus and shear strain:

$$G = \frac{G_{\max}}{1 + \gamma_h}, \tag{7}$$

$$D = \frac{\gamma_h}{1 + \gamma_h} D_{\max}, \tag{8}$$

where G and D are the shear modulus and damping ratio; $G_{\max} = k_2 (\sigma_m^{'})^{n_2}$ is the initial shear modulus; $(\sigma_m^{'})$ is the mean effective stress; $D_{\max}, k_2, n_2$ are experimental parameters.

$$\gamma_h = \left[1 + Ae^{-B\gamma/\gamma_r}\right] \frac{\gamma}{\gamma_r}, \tag{9}$$

where A and B are adjustment factors; $\gamma_r = (\tau_{\max}/G_{\max})$ is the reference strain, with $\tau_{\max}$ as the maximum shear stress.

For the soil in the ash storage field, the shear modulus follows the Hardin–Drnevich model, and thus equation (9) can be modified as

$$\gamma_h = \frac{\gamma}{\gamma_r}. \tag{10}$$

The damping ratio of the soil can be calculated by

$$\frac{\lambda}{\lambda_{\max}} = \left(1 - \frac{G_d}{G_{d\max}}\right)^m. \tag{11}$$

3.1.3. Calculation of the Dynamic Pore Water Pressure. According to dynamic test results, the change of dynamic pore water pressure during vibration follows the following pattern:

$$\frac{u_d}{\sigma_{3c}^{'}} = \frac{1}{2} + \frac{1}{\pi} \arcsin\left[2\left(\frac{N_m}{N_f}\right)^{(1/\theta)} - 1\right], \tag{12}$$

where u_d is the dynamic pore water pressure; σ^{3c} is the effective minor principal stress under initial static condition; N_f is the number of vibrations at failure; N_m is the number of vibrations; θ is the experimental parameter.

The magnitude of shear stress varies with the number of vibrations. The higher the shear stress, the smaller the number of vibrations for soil to reach the failure state. The number of vibrations at failure is related to the dynamic strength of the soil and can be calculated by

$$\frac{\tau_d}{\sigma_{,3c}} = A_1 N_f^{-B_1}, \tag{13}$$

where τ_d is the dynamic shear stress; A_1 and B_1 are experimental parameters.

3.1.4. Determination of Fundamental Frequency of the Dam. The damping ratio of the dam material is generally below 0.22. The dam's self-oscillation frequency can be calculated without taking the damping effect into account

$$[K]\{\delta\} + [M]\left\{\ddot{\delta}\right\} = 0. \tag{14}$$

The characteristic equations for the simple harmonic motion of the masses during free vibration of the dam body are as follows:

$$[K]\{\delta_0\} = \omega^2 [M]\{\delta_0\}, \tag{15}$$

where $\{\delta_0\}$ is the nodal amplitude arrays. The characteristic equations above are n^{th}-algebraic equations, which give the self-oscillation frequencies for each order of the dam body, with the first frequency being used here.

3.1.5. Determination of the Liquefied Zone and Liquefication Criterion. Here, the pore pressure level is used to determine whether liquefaction has occurred; i.e., a unit is considered to have been liquefied if the ratio of the superhydrostatic pressure to the static initial effective minor principal stress is greater than 1.0. Based on the method by Seed and Idriss [21], the dynamic shear stress can be modified as

$$\left(\frac{\tau_d}{\sigma_{3c}^{'}}\right)_{\text{mod}} = K_a K_s \left(\frac{\tau_d}{\sigma_{3c}^{'}}\right)_{\text{test}}, \tag{16}$$

where k_a is the function of the ratio of initial horizontal shear stress to the initial normal stress; k_s is the function of the initial normal stress. Figure 2 presents the correction curves for the above two parameters. After modification of the shear stress, liquefication occurs when the ratio of dynamic pore water pressure to the initial minor principal stress under static condition is greater than 1.0, i.e., $(u_d/\sigma_{3c}^{'}) \geq 0$.

3.2. Geometric Model and Parameters for Numerical Computation. The geometric model used for the numerical computation is consistent with the schematic diagram of the primary dam and subdams of the ash storage field in Figure 1. Depending on the extent of the ash storage field, the geometrical model is shown in Figure 3. It consists of breccias layer, which acts as the foundation of the dam, ash storage field, drainage area and gallery, primary dam, and the three subdams. This study focused on the influence of the length of the dry beach on the dynamic stability of the ash storage field, and therefore, the boundary conditions shown in the red line, i.e., the dry beach, were set at the top of the model. In this study, the length of the dry beach is set to be 0, 50, 100, 150, and 200 m, respectively. According to the literature [22], The parameters for numerical computation were listed in Tables 3 and 4.

3.3. Time Course Curve for Bedrock Acceleration. According to the Peak Earthquake Acceleration Zoning Map of China, the designed bedrock acceleration of this project is 0.2 g (the designed seismic intensity is 8 degrees). The time-course curve of the Wenchuan earthquake was used as the input bedrock acceleration. The duration of the Wenchuan earthquake is 3 minutes, and the seismic waves were processed by selecting the seismic acceleration time curve for 30

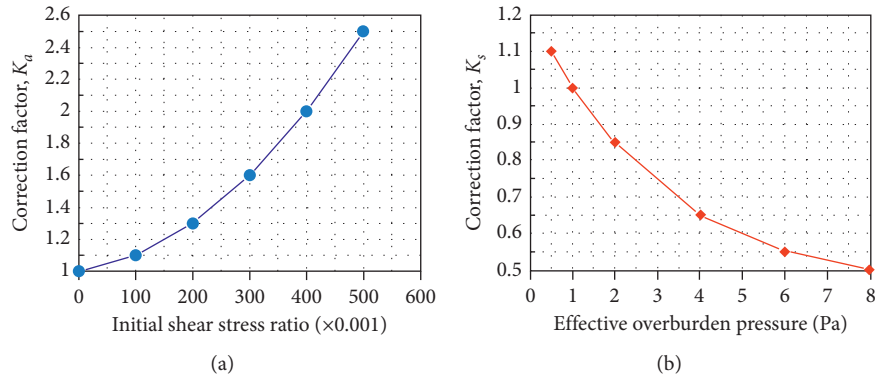

Figure 2: Correction curves for K_s and K_a. (a) Variation of K_a, (b) variation of K_s.

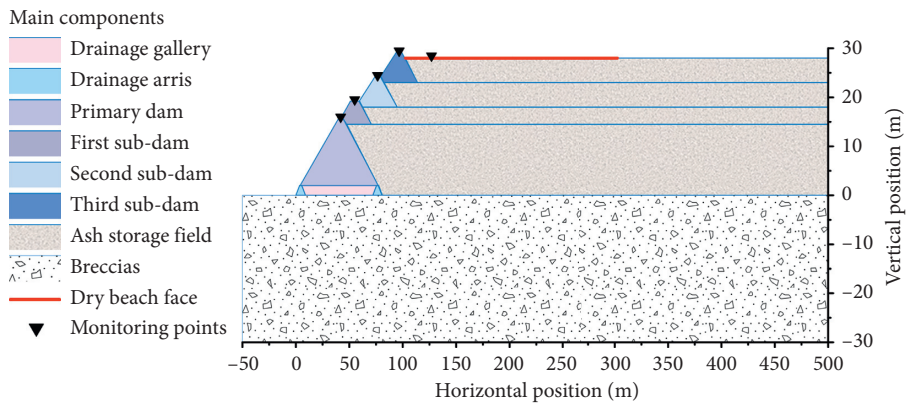

Figure 3: Geometric model for numerical computation.

Table 3: Model parameters for static computation.

Material	Dry density (g/cm^3)	Compressive modulus (MPa)	Strength indexes		Permeability coefficient (cm/s)	K	n	R_f	μ
			c (kPa)	ϕ (°)					
Ash storage field	0.88	3.42	6	25	2.63×10^{-4}	102	0.65	0.8	0.25
Subdam	1.08	23	18	28	0.45×10^{-4}	160	0.81	0.92	0.33

Table 4: Model parameters for dynamic computation.

No	Material	Unit weight, γ (kN/m^3)	k	n	λ_{max}	μ	θ	m	c_d (kPa)	ϕ_d (°)
1	Subdam	15.7	1100	0.74	0.185	0.30	0.83	0.55	12	25
2	Ash storage field	14.8	1000	0.7	0.205	0.35	2.2	0.52	4	20
3	Primary dam	22.6	2133	0.50	0.122	0.28	—	—	46	30
4	Drainage area	22.5	$G = 420$ MPa		0.100	0.26	—	—	0	38
5	Breccias	22.3	2133	0.50	0.122	0.28	—	—	46	30

seconds in the range of the maximum acceleration (Figure 4), whose maximum seismic acceleration is 0.2 g, the duration of the earthquake is 30.0 s, and the maximum acceleration moment is 12.84 s. In this study, as the ash storage site is far from the epicenter of the Wenchuan earthquake, its ground vibration mostly occurs in horizontal direction. In addition, considering the need to select the most unfavorable working conditions, this study assumes that the seismic inertial force acts on the bedrock horizontally perpendicular to the dam axis and that seismic waves propagate from the bedrock towards the dam.

3.4. Numerical Scheme. The computational procedure includes eight main steps:

As the first step, the steady-state seepage of ash storage field and the dams under the considered conditions was

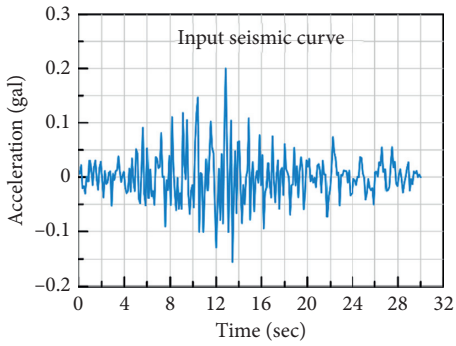

Figure 4: Time course curves for bedrock seismic acceleration.

calculated as the initial static pore pressure field for the dynamic liquefaction calculation.

The second step is to calculate the stress field of the ash storage field and the dam under static stress, which will be used as the initial stress field for the dynamic response analysis. A finite element model for static calculations was built, and the parameters and bulk weight of the E-μ nonlinear constitutive model of the soil were input, with the calculated boundary conditions applied and the convergence conditions entered.

In the third step, the initial static pore pressure field and the initial static stress field were introduced for dynamic response calculation. The finite element model identical to that under static stress condition was built with the equivalent viscoelastic model parameters and corresponding curves input, and boundary conditions were applied for dynamic computation. The initial static stress field was introduced, and the convergence conditions for numerical computation were specified. The time-course acceleration curves and the maximum acceleration were input and used to calculate the dynamic response of the dam and the ash storage field.

In the fourth step, assuming the initial values of the dynamic shear modulus G_d and the damping ratio λ for each element (determined by the test according to the estimated strain range), the shear strain vs. time curve for the computational time (divided into smaller timesteps for the time of Δt) was calculated, and the average shear strain (0.65% of the maximum strain) for each element for the time was obtained.

In Step 5, the corresponding dynamic shear modulus G_d based on this average shear strain was calculated. If it does not match the assumed initial value, readjust G_d and λ and perform iterative calculations again until the criterion is satisfied, i.e., $(G_d^{i-1} - G_d^i/G_d^i) \le 0.1$. The magnitude of the shear strain for each element at time t was obtained with the mean shear stress $\tau_v = 0.65\tau_{\max}$ and the initial shear stress ratio τ_v/σ_0.

In the sixth step, the number of equivalent cycles ΔN for the period was determined, and based on this ΔN and the shear strain amplitude of each element, the corresponding pore water pressure increments and cumulative pore pressure were determined from the selected pore pressure model.

In the seventh step, the effective stress state of each element corresponding to the practical pore water pressure level was determined, the corresponding initial dynamic shear modulus G_{d0} was calculated, and the new stress strain was obtained from the substituted equivalent viscoelastic model.

In Step 8, repeat the above calculations for the next timestep until the earthquake is over.

4. Analysis of Dynamic Response of Ash Storage Field

4.1. Acceleration of the Ash Storage Field. Figure 5 presents the contour of acceleration in various parts of the ash storage field at different dry beach lengths. The acceleration in the ash storage field is relatively small in the breccias layer, increases with height and peaks near the third subdam, and tends to decrease from the subdams towards the ash storage area. The peak acceleration in the ash storage area occurs at a similar position near the third subdam as the length of the dry beach increases, but the values increase with the length of the dry beach. At the same time, the acceleration in the ash storage area near the surface increases, and, significantly, the range where the higher accelerations appear also increases.

The acceleration vs. time curves for five different parts of the ash storage field (i.e., the top of the third, second, first subdams and the primary dam, and inside the ash storage area at a distance of 25 m from the third subdam) were plotted for two cases with dry beach lengths of 0 m and 150 m, respectively, as shown in Figure 6. It is evident that, after inputting the time-course curve of acceleration during the Wenchuan earthquake, significant acceleration responses are exhibited within the three subdams, the primary dam, and the ash storage area with alluvial fly ash. As shown in Figure 6(a), in the absence of a dry beach surface ($L_d = 0$ m), the peak acceleration at the crest of the third subdam at relatively high altitudes is the highest at about 0.237 g. The first and second subdams and the primary dam at relatively low altitudes gradually decrease, with the lowest acceleration within the ash storage area at about 0.196 g. When a dry beach is present, such as in the 150 m dry beach case shown in Figure 6(b), the acceleration response of the various parts of the ash storage field is also very significant. Compared to the case with no dry beach, the maximum acceleration in the interior of the ash storage field (alluvial ash) is about 0.227 g. The peak acceleration at the crest of the third subdam (0.219 g) is smaller, and the peak accelerations at the primary dam and the first and second subdams are the lowest. It is apparent that the dry beach has a small effect on the time-course curves of the acceleration of the various parts of the ash storage field, but it has a significant effect on the peak acceleration, which is reflected in the fact that as the length of the dry beach increases, the response of the peak acceleration is more pronounced for the third subdam and within the ash storage field, and less so for the rest of the field. More specifically, this can be seen in the histograms of

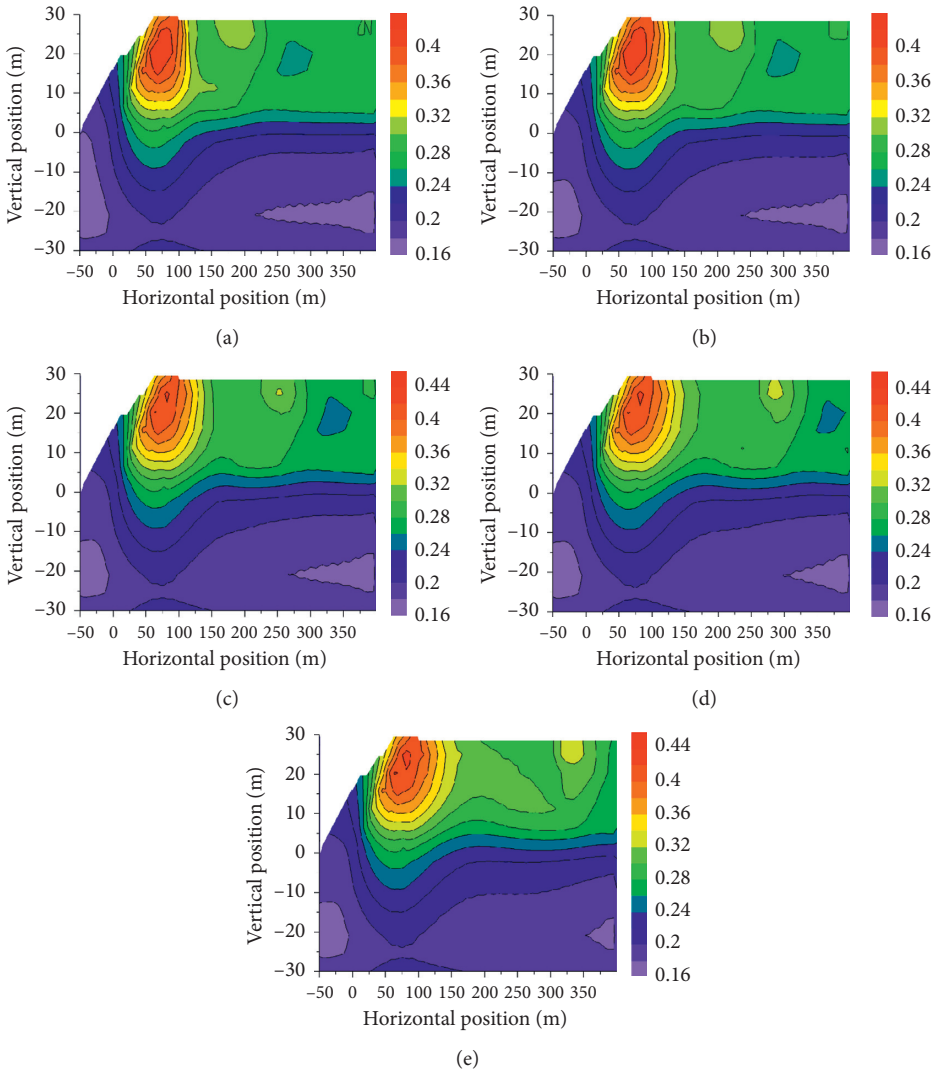

Figure 5: Contour of acceleration of various parts of the ash storage field. (a) $L_d = 0$ m, (b) $L_d = 50$ m, (c) $L_d = 100$ m, (d) $L_d = 150$ m, (e) $L_d = 200$ m.

peak acceleration at various parts of the ash storage field under different dry beach lengths shown in Figure 7.

4.2. Horizontal Displacement of the Ash Storage Field. From the calculated horizontal displacement of various parts of the ash storage field, the maximum values of the ash storage field and the dam occur at 13.32 s, although the peak acceleration of the Wenchuan seismic acceleration imposed by the boundary conditions at the bottom of the model is at 12.84 s. Figure 8 gives the contour of the horizontal displacements at various parts of the ash storage site. Clearly, as it shows that the maximum horizontal displacements at different dry beach lengths occur at the crest of the third subdam and in the adjacent ash storage area, as the length of the dry beach increases, the maximum horizontal displacements show a certain decrease in value, but they occur progressively further away from the third subdam, so that, under dynamic forces, the dam becomes safer as the dry beach length increases.

The horizontal displacement time-course curves for five different parts of the ash storage site (the top of the third subdam, the second subdam, the first subdam, the primary dam, and the ash storage area at 25 m from the third subdam) were plotted for two cases with dry beach lengths of 0 m and 150 m, as shown in Figure 9. It is observed that, after the input of the time-course curve of the acceleration of the Wenchuan earthquake, all the subdams, primary dam, and the alluvial ash storage field exhibit an evolving horizontal displacement response to the input acceleration, which appears to be slightly delayed overall. As shown in Figures 9(a) and 9(b), for the five selected different positions of the ash storage sites, the largest horizontal displacements occur within the ash storage field, slightly larger than those at the top of the subdams, with the smallest horizontal displacements being at the primary dam. In addition, a comparison of the two dry beach lengths shows that the formation of a dry beach can significantly

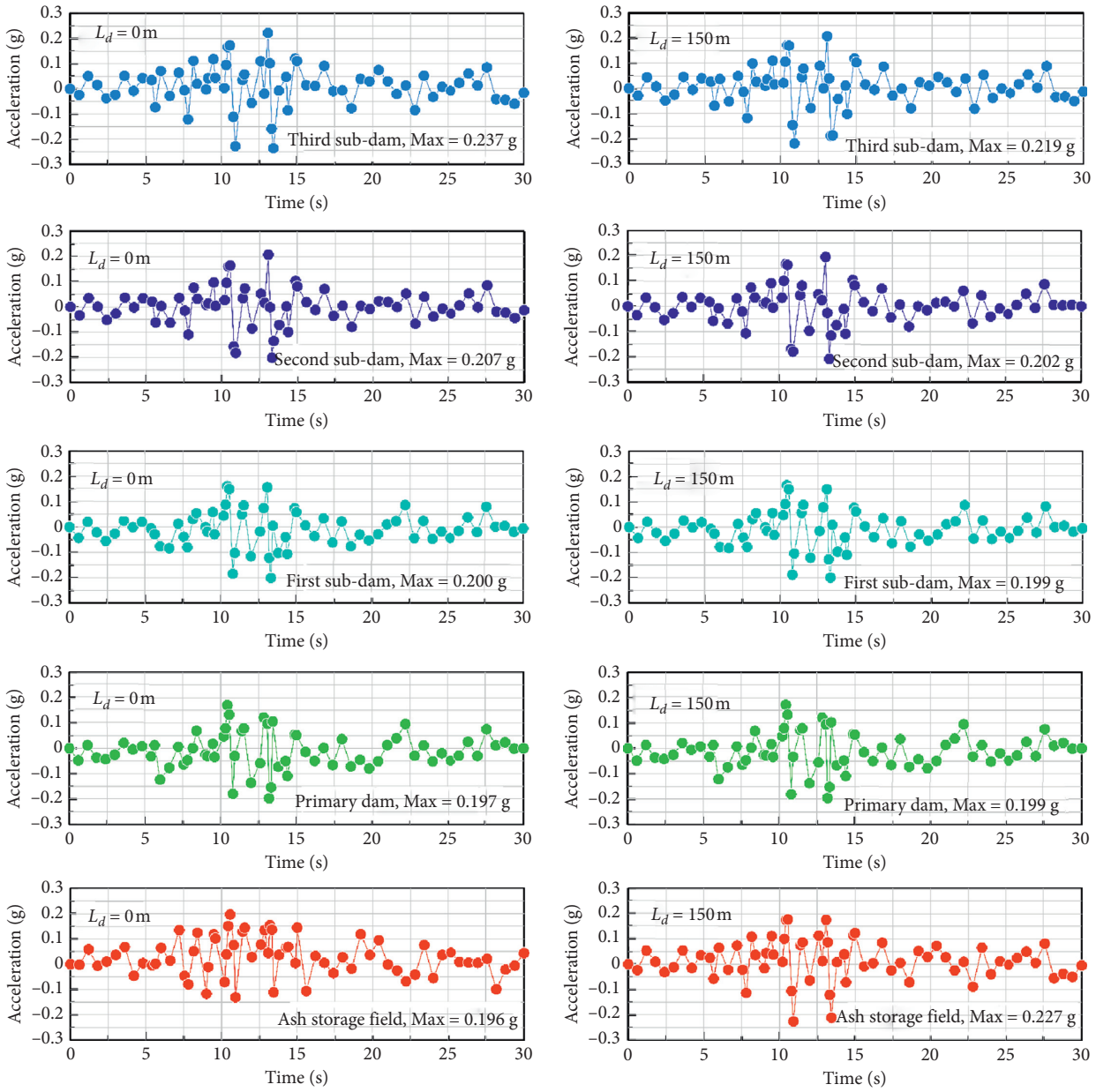

Figure 6: Time-course curves of acceleration of various parts of the ash storage field.

suppress horizontal displacements, especially in the alluvial ash storage field.

In addition, we also plotted the maximum horizontal displacements at five different positions of the ash storage site with different dry beach lengths, as shown in the horizontal displacement histogram for each location of the storage site in Figure 10. It is clear that the maximum horizontal displacement at the five different sites occurs within the ash storage field, followed by the top of the third subdam, the top of the second subdam, the top of the first subdam, and the minimum value at the top of the primary dam. The horizontal displacements at the primary dam do not vary much with different beach lengths. For the rest of the ash storage site, the maximum horizontal displacement decreases as the beach length increases.

4.3. Analysis of Liquefied Zone in the Ash Storage Field. Liquefaction is the condition and process by which a saturated soil is transformed into a liquid state under vibration or shock loads. When earthquakes or vibrations act on the soil, the load is mainly borne by water in the pores, causing a sudden increase in the dynamic pore water pressure, a decrease in the effective stress, and a loss of strength. The moment at which the seismic action ends is the moment of maximum dynamic bore pressure and the moment of maximum liquefaction, so the effective stress at the end of the seismic action is chosen for analysis, as shown in Figure 11. The red area in the diagram shows the liquefaction range in the ash storage field. Here, the range of effective stresses below 0 kPa has been chosen as the liquefaction zone. As the length of the dry beach increases, the

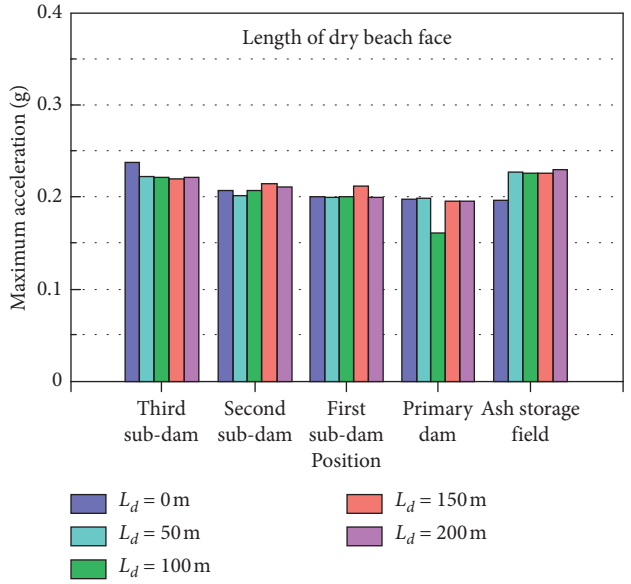

Figure 7: Peak acceleration of various parts of ash storage field at different dry beach lengths.

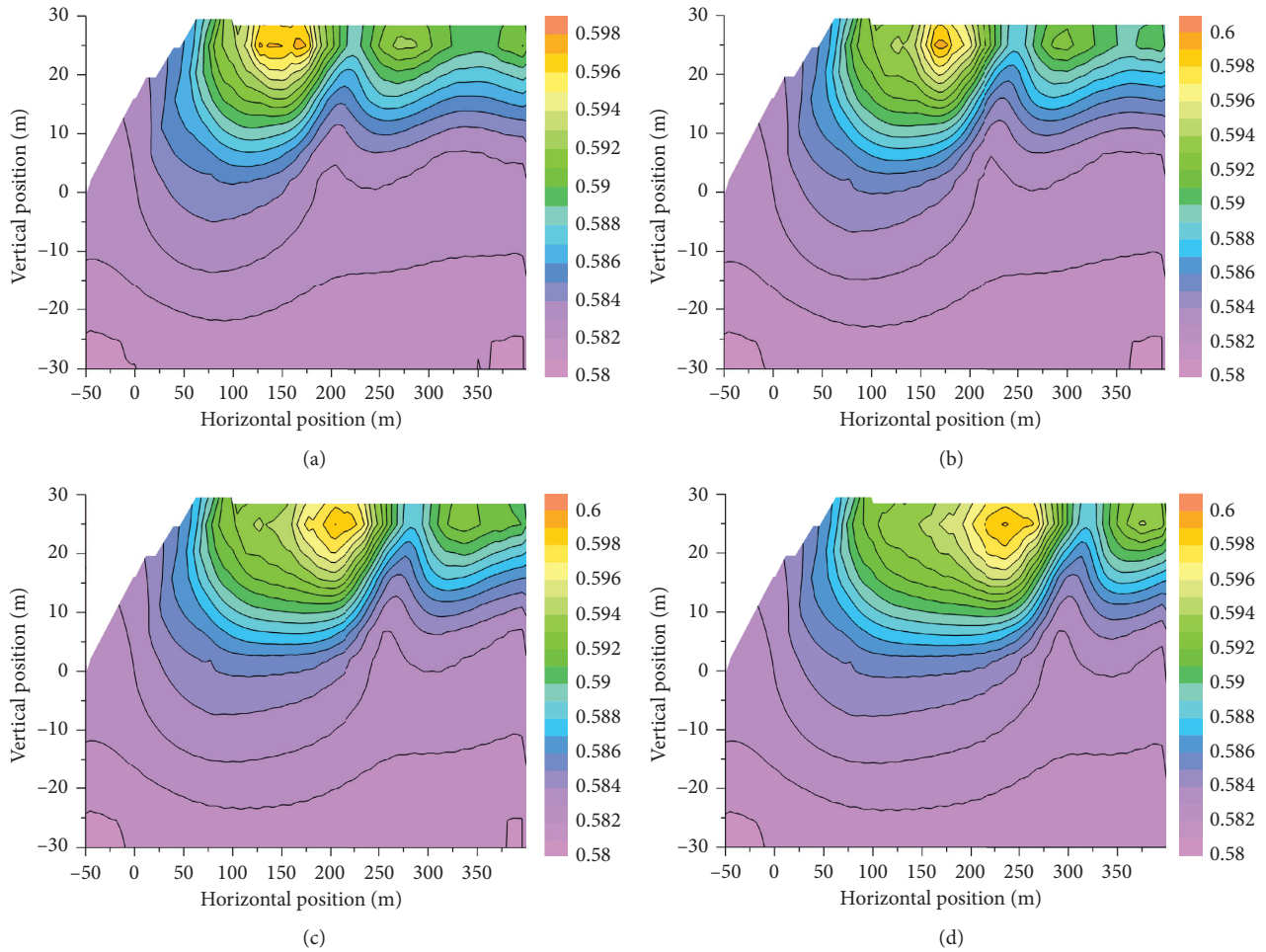

Figure 8: Continued.

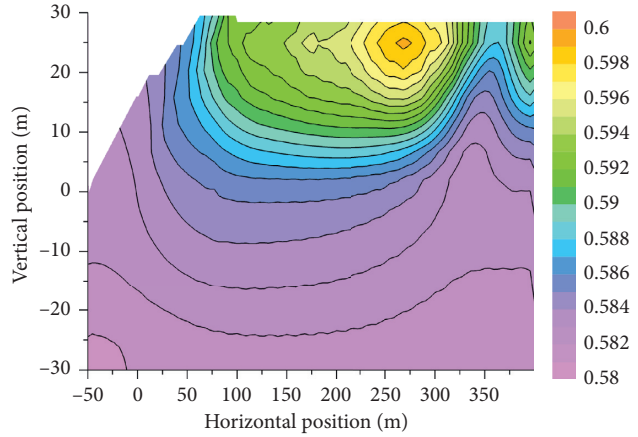

(e)

Figure 8: Contour of horizontal displacement of various parts of the ash storage field. (a) $L_d = 0$ m, (b) $L_d = 50$ m, (c) $L_d = 100$ m, (d) $L_d = 150$ m, (e) $L_d = 200$ m.

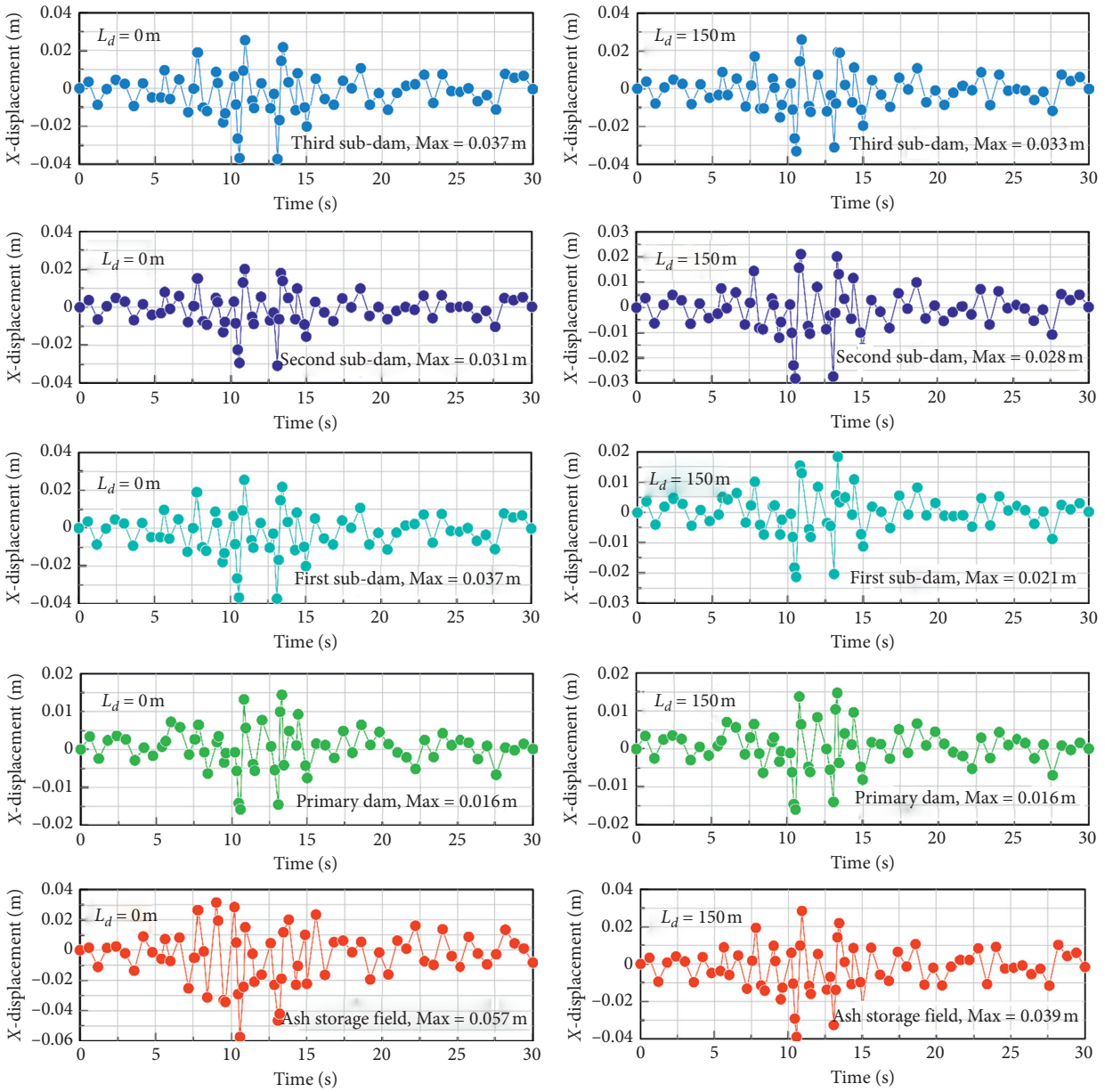

Figure 9: Time-course curves of horizontal displacement of various parts of the ash storage field.

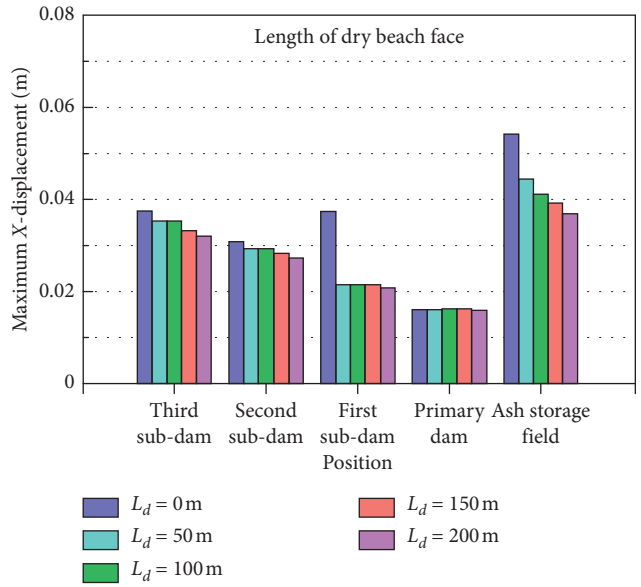

Figure 10: Horizontal displacement of various parts of the ash storage field at different dry beach lengths.

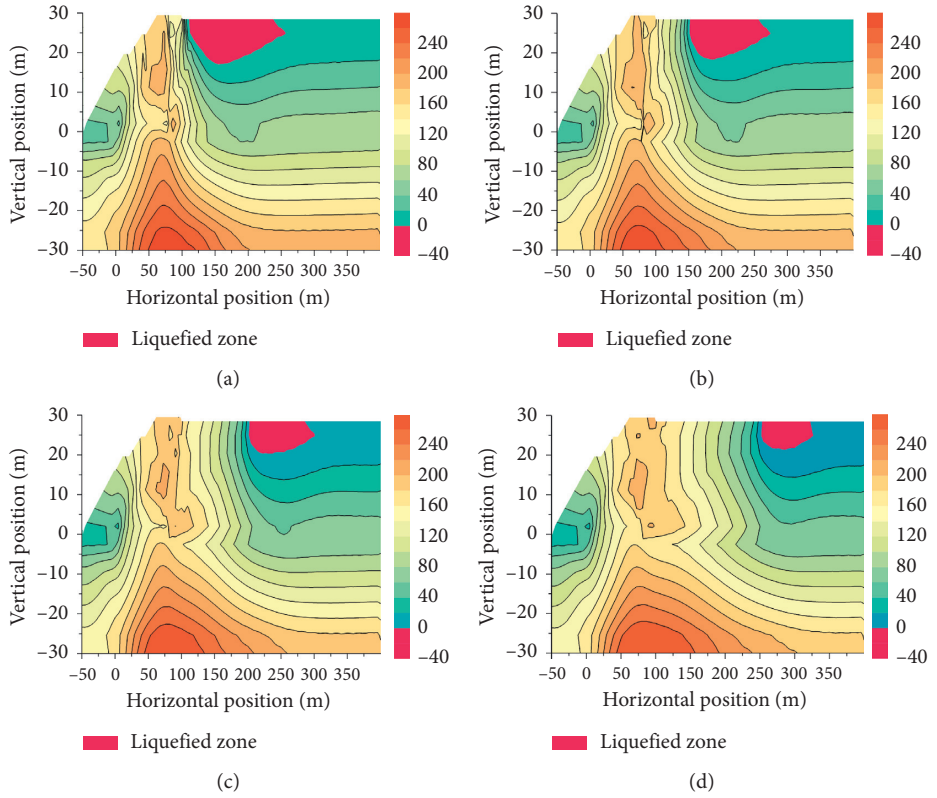

Figure 11: Continued.

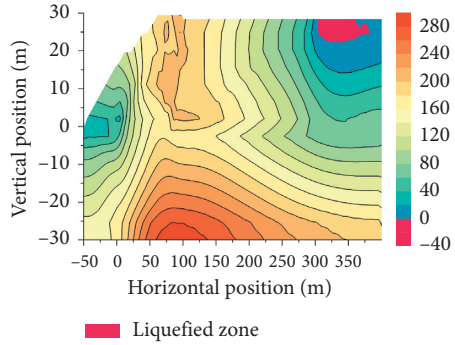

Figure 11: Contour of effective stress in the ash storage field and the liquefied zone. (a) $L_d = 0$ m, (b) $L_d = 50$ m, (c) $L_d = 100$ m, (d) $L_d = 150$ m, (e) $L_d = 200$ m.

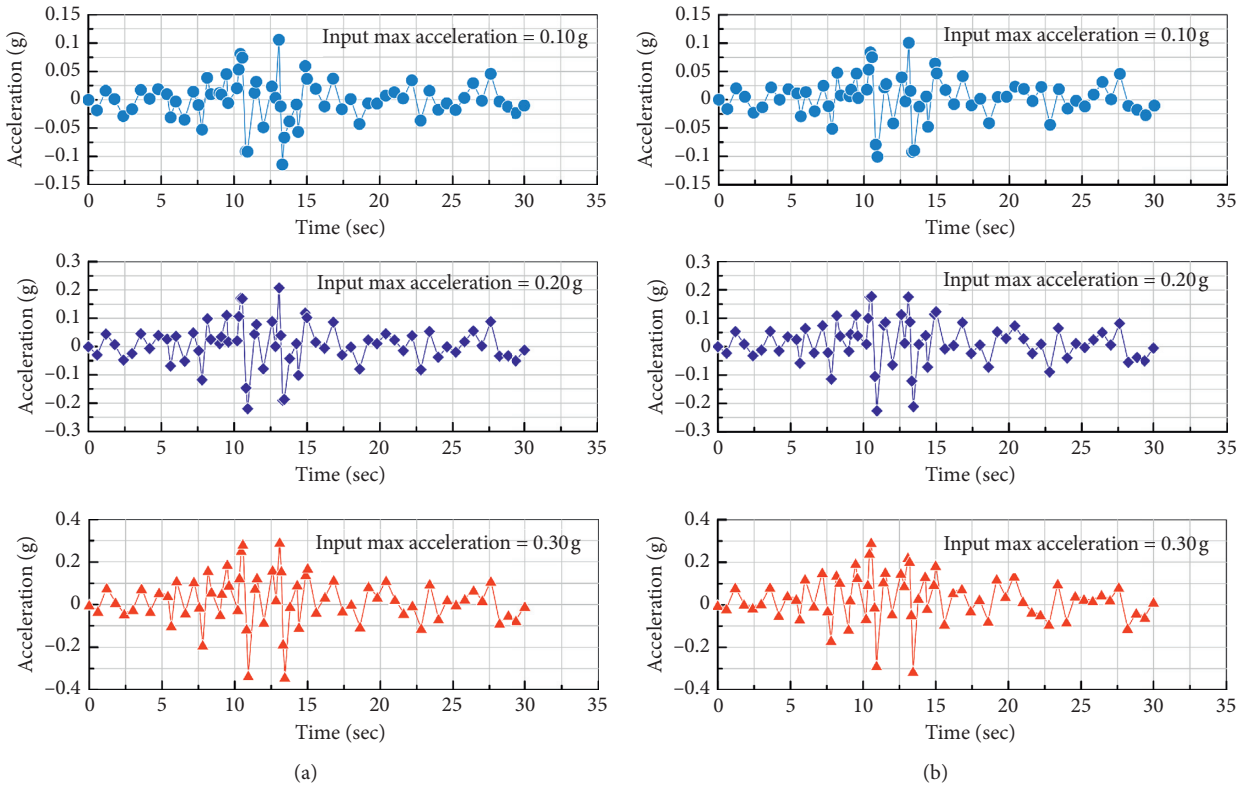

Figure 12: Time-course curves of acceleration of the third subdam and ash storage field under three input earthquakes ($L_d = 150$ m). (a) Third subdam. (b) Ash storage field.

liquefaction zone gradually decreases, and the liquefaction zone extends further away from the third subdam and into the alluvial ash storage field.

A further notable feature is that the area of liquefaction at the end of the seismic event shows that the geomembrane impermeability of the subdams at all levels and the good drainage of the primary dam, the absence of liquefaction at all levels and the primary dam, and the liquefaction of the ash deposited in the ash storage field occur at the shallow end of the maximum limiting storage elevation. The depth of the liquefaction range decreases as the length of the dry beach increases. It is, therefore, recommended that the dry beach length of this ash storage site should not be less than 150 m.

4.4. Influence of the Input Peak Acceleration on the Horizontal Displacement and the Range of Liquefied Zone. In order to further analyze the influence of the input ground acceleration on the dynamic response of the ash storage site, the time-course curves of the input ground acceleration with peak accelerations of 0.10 g and 0.30 g have been selected by reducing or amplifying the bedrock seismic acceleration

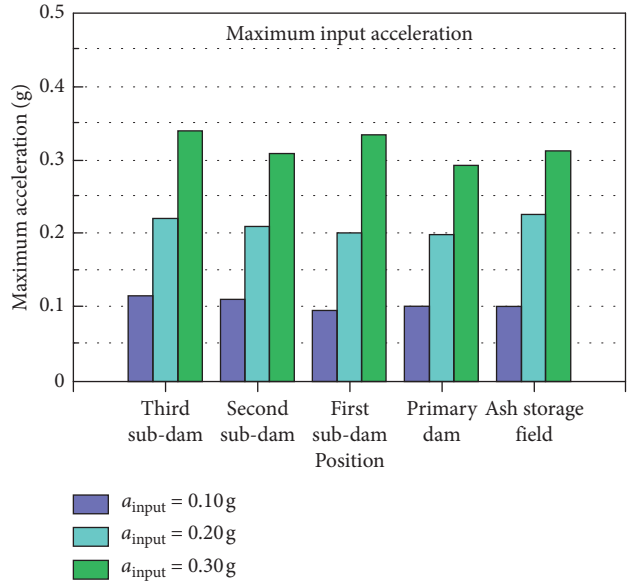

Figure 13: Peak acceleration of various parts of ash storage site under three input earthquakes (L_d = 150 m).

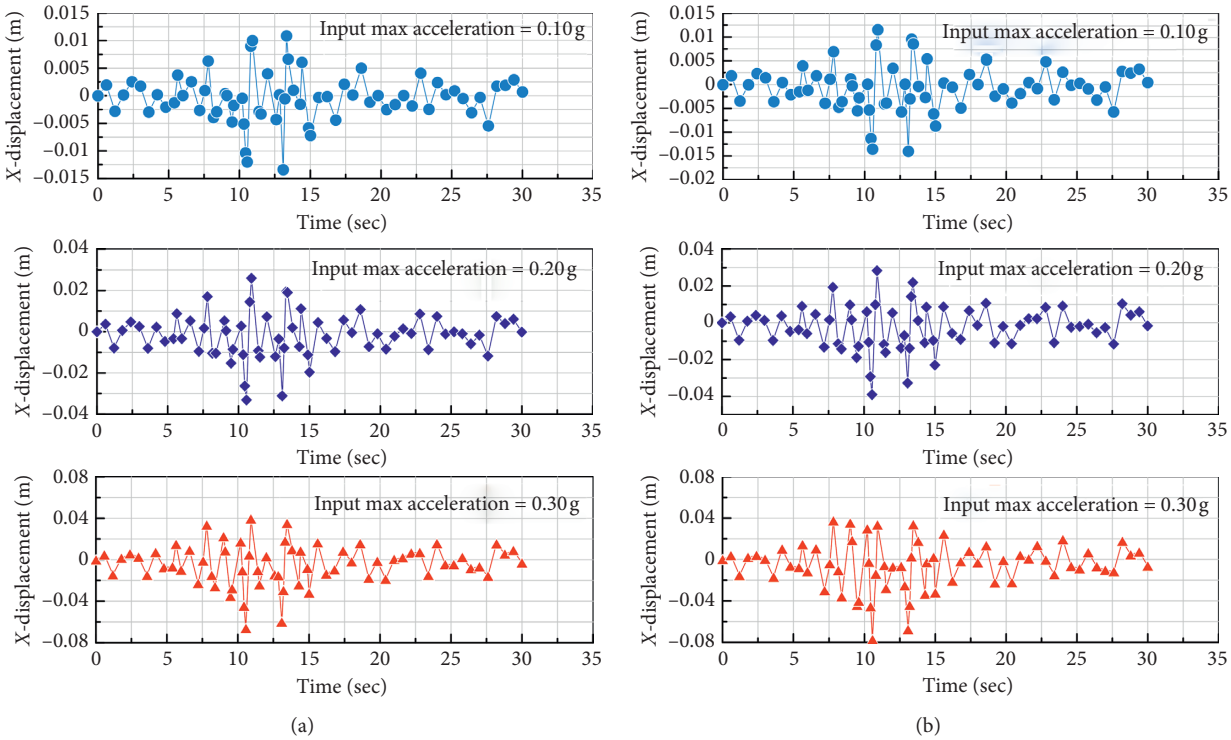

Figure 14: Time-course curves of horizontal displacement of third subdam and ash storage field under three input earthquakes (L_d = 150 m). (a) Third subdam. (b) Ash storage field.

time curves shown in Figure 4, respectively. The dynamic response of an ash storage site with a dry beach face length of 150 m for two input earthquakes was recalculated after entering it into the program. Figure 12 presents the time-course curves of the acceleration for two parts of the third subdam and the alluvial ash storage field under three types of input ground acceleration (peak acceleration of 0.10 g, 0.20 g, and 0.30 g). In addition, the difference in dynamic response between the two selected sites is relatively small. This phenomenon can also be seen in the histogram of Figure 13 of the peak acceleration response at five different positions for three input ground accelerations.

Figure 14 illustrates the time-course curves of horizontal displacements (L_d = 150 m) for the third subdam and the storage field for three different input earthquakes. For a given ash storage site, the time-course curve of the

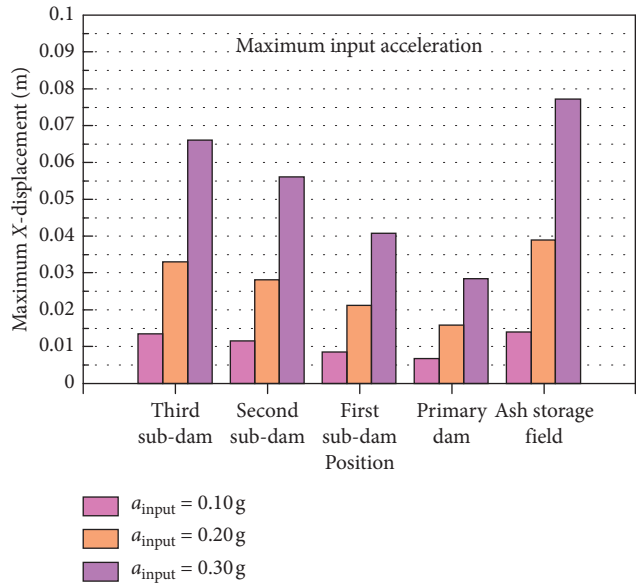

FIGURE 15: Peak horizontal displacement of various parts of ash storage site under three input earthquakes (L_d = 150 m).

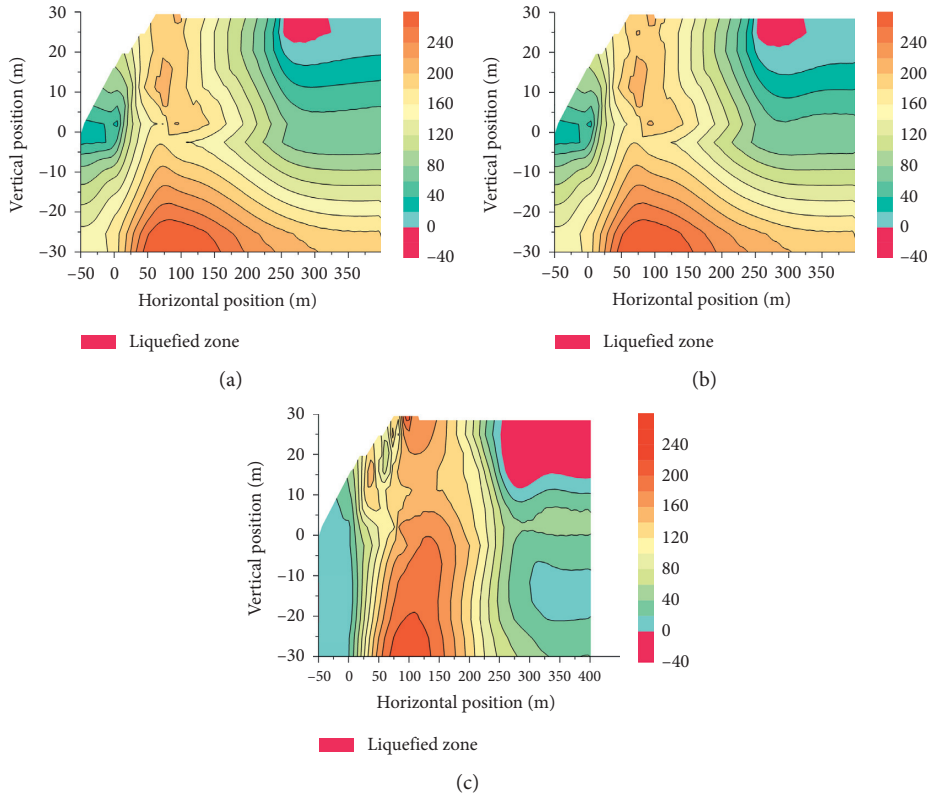

FIGURE 16: Contour of effective stress and range of liquefied area of ash storage site under three input earthquakes (L_d = 150 m). (a) a_{max} = 0.10 g. (b) a_{max} = 0.20 g. (c) a_{max} = 0.30 g.

horizontal displacement can be seen to exhibit significant fluctuations, which are closely related to the temporal variation of the input ground acceleration. The peak horizontal displacement at the selected site increases significantly with increasing peak acceleration of the input ground acceleration, which can be clearly seen in Figure 15. In addition, of the five selected ash storage positions, the peak horizontal displacement within the ash storage field is the highest, which is due to the relatively weaker mechanical properties of the alluvial fill material within the storage field

compared to the compacted soils of the subdams and primary dams. Another phenomenon is that peak horizontal displacement in the third subdam is slightly lower than that in the ash storage field monitoring position, but it is significantly higher than that in the remaining subdams and primary dams. As the filling height decreases, the peak horizontal displacement decreases progressively, and this phenomenon is observed for all three input earthquakes considered. The higher the peak acceleration of the input ground acceleration is, the more pronounced this phenomenon becomes.

Figure 16 presents the contour of the effective stress distribution and the range of the liquefied area in an ash storage field with 150 m dry beach length under three input earthquakes. It is noted that the effective stress distribution, the area enclosed by the liquefied area, and its distance from the three-stage subdam do not change significantly at the two input earthquakes of 0.10 g and 0.20 g, but at a peak acceleration of 0.30 g in the input earthquake, the liquefied area increases significantly, even through the center of the storage field. This also means that, for an ash storage site with a dry beach length of 150 m, the first two types of input ground shaking considered do not have a significant effect on the liquefaction range in the ash storage site and that the liquefaction range changes significantly as the input acceleration of the ground acceleration increases. Other measures should be taken to maintain the dynamic stability of the dam and the ash storage field, such as the improvement of drainage facilities.

5. Conclusions

This study carried out a dynamic response analysis of an ash storage site in northwest China, using the Wenchuan seismic waves as input ground shaking, and investigated the effect of dry beach length on the horizontal displacement, peak acceleration, and liquefaction range of the site. The main conclusions are as follows.

(1) In situ standard penetration tests at all levels of subdams, primary dams, and alluvial ash in the ash storage field have shown that areas of liquefaction do not occur at all levels of subdams but may occur in the alluvial ash storage area and should be dealt with, for example, by strengthening drainage facilities.

(2) The acceleration in the ash storage field is relatively low in the breccias layer but increases with height, with the peak acceleration occurring in the vicinity of the third subdam and tending to decrease from the subdams towards the alluvial ash storage area. At a larger dry beach length, the peak acceleration occurs at similar locations within the ash storage area but increases with dry beach length.

(3) The maximum horizontal displacements of the different dry beach lengths occur at the crest of the third subdam and in the adjacent ash storage area. At a larger dry beach length, the maximum horizontal displacement decreases but occurs progressively further away from the third subdam, so that, under dynamic forces, the dam becomes safer. The extent of liquefaction also decreases and extends further away from the third subdam and into the ash storage field. It is, therefore, recommended that the dry beach length should not be less than 150 m for this ash storage site.

Data Availability

The data used to support the findings of this study are available from the corresponding author upon request.

Conflicts of Interest

The authors declare no conflicts of interest.

Acknowledgments

The research described in this paper was financially supported by the National Natural Science Foundation of China (Grant nos. 51608442 and 51778528), the Basic Research Program of Natural Science of Shaanxi Province (Grant No. 2019JLM-56), and the Research Fund of the State Key Laboratory of Eco-hydraulics in Northwest Arid Region, Xi'an University of Technology (Grant No. 2019KJCXTD-12). These supports are greatly appreciated.

References

[1] M. D. A. Thomas, "Field studies of fly ash concrete structures containing reactive aggregates," *Magazine of Concrete Research*, vol. 48, no. 177, pp. 265–279, 1996.

[2] R. L. Parsons and E. Kneebone, "Field performance of fly ash stabilised subgrades," *Ground Improvement*, vol. 9, no. 1, pp. 33–38, 2005.

[3] M. Izquierdo, X. Querol, A. Josa, E. Vazquez, and A. López-Soler, "Comparison between laboratory and field leachability of MSWI bottom ash as a road material," *Science of the Total Environment*, vol. 389, no. 1, pp. 10–19, 2008.

[4] R.-U.-D. Nassar, P. Soroushian, and T. Ghebrab, "Field investigation of high-volume fly ash pavement concrete," *Resources, Conservation and Recycling*, vol. 73, pp. 78–85, 2013.

[5] X. H. He, "Analysis of dynamic leaching test about heavy metals in solidification body of municipal solid waste incineration fly ash," *Nature Environment and Pollution Technology*, vol. 15, no. 4, pp. 1199–1204, 2016.

[6] P. J. Amaya, J. T. Massey-Norton, and T. D. Stark, "Evaluation of seepage from an embankment dam retaining fly ash," *Journal of Performance of Constructed Facilities*, vol. 23, no. 6, pp. 406–414, 2009.

[7] T. S. Sakib, S. Sultana, A. N. Ahmed, M. A. A. Khan, and M. S. Saha, "Water quality of coal ash pond and its impact on adjoining surface and groundwater systems," *American Journal of Water Resources*, vol. 6, no. 4, pp. 176–180, 2018.

[8] V. W. Y. Tam, D. Rahme, I. M. Chethana, L. Le, and J. Yu, "Effective remediation strategies for ash dam sites in coal power plants," *Engineering Sustainability*, 2020.

[9] J. C. Santamarina, L. A. Torres-Cruz, and R. C. Bachus, "Why coal ash and tailings dam disasters occur," *Science*, vol. 364, no. 6440, pp. 526–528, 2019.

[10] M. Li, L. Liang, J. Zhao et al., "Dynamic response and liquefaction analysis of large ash storage dam," *Journal of Northeastern University*, vol. 28, no. 12, pp. 1766–1769, 2007.

[11] G. X. Wang and Z. Z. Wang, "Dynamic response analysis of fly ash dam," *Chinese Journal of Geotechnical Engineering*, vol. 10, no. 5, pp. 87–92, 1988.

[12] S. J. Hu, "On liquefaction and dynamic stability of ash dam," *Journal of Zhejiang University (Natural Science Edition)*, vol. 22, no. 5, pp. 43–50, 1988.

[13] J. Zhou, Y. Chi, and P. J. Qi, "3-D dynamic analysis of Taiyuan fly ash dam," in *Proceedings of the International Conferences on Recent Advances in Geotechnical Earthquake Engineering and Soil Dynamics*, no. 5, San Diego, CA, USA, March 2001.

[14] H. B. Liu, H. B. Wei, and Y. P. Gao, "Experimental research on dynamic properties of fly ash soil and silty clay after freeze-thaw cycling," in *Proceedings of the International Conference on Transportation Engineering 2007*, pp. 4105–4111, Chengdu, China, July 2007.

[15] L. Dong, *Study on Dynamic Characteristics of Fly Ash Mixed with Soil*, Northwest Agriculture and Forestry University, Xianyang, China, 2009.

[16] Z. P. Wang, "Influence of fly ash content on dynamic characteristics of loess," *Northwest Agriculture and Forestry University*, 2016.

[17] J. Wang, Q. Wang, P. Wang et al., "Effects of fly ash incorporation on dynamic constitutive relation of modified loess," *Chinese Journal of Geotechnical Engineering*, vol. 35, no. S1, pp. 156–160, 2013.

[18] Z. Zhang, M. M. Jiang, and C. Z. Guo, "Characteristics of liquefaction and dynamic modulus weakening of coal ash under earthquake action," *Concrete*, no. 6, pp. 88–92, 2017.

[19] Z. Li, Y. S. Luo, and Y. C. Xing, "Experimental study on dynamic characteristics of fly ash under dynamic torsional shear load," *Journal of Rock Mechanics and Engineering*, vol. 25, no. S1, pp. 3080–3086, 2006.

[20] H. B. Wei, H. B. Liu, Y. P. Gao et al., "Experimental study on dynamic characteristics of fly ash soil after freeze-thaw cycles," *Rock and Soil Mechanics*, vol. 28, no. 5, pp. 1005–1008, 2007.

[21] H. B. Seed and I. M. Idriss, "Influence of soil conditions on ground motions during earthquake," *Journal of the Soil Mechanics and Foundations Division*, vol. 95, no. 1, pp. 99–137, 1969.

[22] F. She, S. Wang, J. Li, J. Ding, and Q. Wang, "Experimental study of dynamic characteristics of fly ash in ash storage dams," *China Earthquake Engineering Journal*, vol. 40, no. 5, pp. 1018–1025.